Ionospheric variation during pulsating aurora

K. Hosokawa[1,2] and Y. Ogawa[3,4]

[1] Department of Comm. Eng. and Informatics, Univ. of Electro-Communications, Tokyo, Japan
[2] Center for Space Science and Radio Engineering, Univ. of Electro-Communications, Tokyo, Japan
[3] National Institute of Polar Research, Tokyo, Japan
[4] SOKENDAI (The Graduate University for Advanced Studies), Kanagawa, Japan

Correspondence

Keisuke Hosokawa
Department of Communication Engineering and Informatics
University of Electro-Communications, Tokyo 182-8585, Japan
Tel: +81 424 43 5299
Fax: +81 424 43 5293
keisuke.hosokawa@uec.ac.jp

For submission to *Journal of Geophysical Research - Space Physics (PsA Special Section)*

Abstract. We have statistically analyzed data from the European Incoherent SCATter (EISCAT) UHF/VHF radars in Tromsø (69.60°N, 19.20°E), Norway to reveal how the occurrence of pulsating aurora (PsA) modifies the electron density profile in the ionosphere. By checking 5 winter seasons (2007-2012) observations of all-sky aurora cameras of National Institute of Polar Research (NIPR) in Tromsø, we have extracted 21 cases of PsA. During these PsA events, either UHF or VHF radar of EISCAT was operative and the electron density profiles were obtained along the field-aligned or vertical direction near the zenith. From these electron density measurements, we calculated h_mE (E region peak height) and N_mE (E region peak density), which are proxies for the energy and flux of the precipitating PsA electrons, respectively. Then, we examined how these two parameters changed during the evolution of 21 PsA events in a statistical fashion. The results can be summarized as follows: (1) h_mE is lower (the energy of precipitation electrons is higher) during the periods of PsA than that in the surrounding interval, (2) When N_mE is higher (flux of PsA electrons is larger), h_mE tends to be lower (precipitation is harder), (3) h_mE is lower and N_mE is larger in the later magnetic local time, (4) When the AE index during the preceding substorm is larger, h_mE is lower and N_mE is larger. These tendencies are discussed in terms of the characteristics of particles and plasma waves in

the source of PsA in the magnetosphere. In addition to the statistics of the EISCAT data, we carried out several detailed case studies, in which the altitude profiles of the electron density were derived by separating the ON and OFF phases of PsA. This allows us to estimate the true altitude profiles of the PsA ionization, which can be used for estimating the characteristic energy of the PsA electrons and better understanding the wave-particle interaction process in the magnetosphere.

1 Introduction

Pulsating aurora (PsA) are diffuse auroral structures often observed in the morning side auroral region typically during the recovery phase of auroral substorms [*Lessard*, 2012 and references therein]. PsA are characterized by their pulsating nature whose period ranges from a few to a few tens of seconds [*Johnstone*, 1983]. The spatial structure of PsA shows a wide variety of shapes, but, in general they are composed of diffuse patches with irregular shape [*Yamamoto et al.*, 1988] or relatively thin arcs somewhat elongated in the east-west direction [*Sato et al.*, 2004]. It is now well accepted that PsA are optical manifestations of quasi-periodic modulation of the flux of precipitating high-energy electrons with energies from a few to a few tens of keV [*Sandahl et al.*, 1980]. It is also widely believed that such high-energy incident electrons are precipitated by the pitch angle scattering through cyclotron resonance with plasma waves near the equatorial plane of the magnetosphere [see a review by *Li et al.*, 2012]. However, we have not yet exactly understood the processes which determine the pulsating period and the shape of PsA patches. In addition, it is still unclear how the quasi-periodic precipitation of the PsA electrons impacts the electron density in the lower part of the ionosphere.

Although PsA have a long history of research since 50's, there have been only a few case studies of PsA by using data from incoherent scatter (IS) radars. *Wahlund et al.* [1989]

first employed the European Incoherent SCATter (EISCAT) radar in Tromsø in Norway for detecting ionization associated with PsA. Later, *Bosinger et al.* [1996] used the EISCAT data to observe the altitude profile of the electron density during PsA, and showed a layer of ionization possibly associated with the PsA electrons. In these early studies, however, the quality and temporal resolution of the electron density estimates were insufficient for resolving the electron density variations during a sequence of the ON and OFF phases of PsA. Recently, *Jones et al.* [2009] employed an IS radar in Poker Flat, Alaska to observe ionization due to PsA and succeeded in estimating the energy distribution of the PsA electrons. However, the temporal resolution of their radar measurements was still not enough to resolve the pulsating period; thus, their analysis provided average altitude profiles of the PsA ionization over the pulsating ON and OFF phases.

More recently, *Hosokawa et al.* [2010] carried out high-time resolution measurements of the electron density during PsA by using the EISCAT radar. Through the analysis of 0.44 sec temporal resolution electron density data, they identified clear modulation of the electron density in the lower E region during an interval of intense PsA. In their data, the electron density varies in harmony with optical pulsations detected by a white-light all-sky camera simultaneously operated in Tromsø. They also discovered a pulsation in the horizontal electric field in the vicinity of PsA patches. This electric field modulation was interpreted as a polarization electric field caused by the enhanced conductivity within the PsA patches. By compiling these observational facts, *Hosokawa et al.* [2010] suggested that the conductivity anomaly within PsA patches is able to modify the electrodynamics in the E region altitudes, which may affect the magnetosphere-ionosphere coupling system above PsA patches. *Hosokawa and Ogawa* [2010] analyzed the data from the same interval of PsA and demonstrated that the electron density in the upper part of the D-region (85–95 km) was significantly enhanced during the PsA. They indicated that such an abnormal ionization can create a layer of Pedersen current carried by electrons in the D region, which may further alter the current system in the ionosphere.

As mentioned above, there have been several recent efforts to study the ionospheric variation associated with PsA using IS radars. To date, however, there have been no statistical studies of the PsA ionization using a large dataset of IS radar; thus, we do not exactly know how the altitude profile of the electron density can be modified by the occurrence of PsA. In addition, it is still unclarified how the PsA ionization is dependent on the magnetic local time (MLT) and the level of magnetic disturbance (e.g., AE index). A statistical analysis for revealing such dependences is highly demanded to better understand the typical and average characteristics of the PsA ionization. In order to conduct such a statistical analysis, we have checked through the simultaneous observations of the EISCAT radar and several all-sky cameras in Tromsø during 5 winter seasons from 2007 to 2012. As a result, we identified 21 examples of simultaneous measurements of PsA with the radar and optics. By using these datasets, we investigated the altitude profile of the PsA ionization in a statistical fashion. In addition to the statistics, we carried out a few detailed case studies in which the altitude profiles of the electron density are examined by separating the ON and OFF phases of PsA. This allows us to derive the true (not average) altitude profile of the PsA ionization, which provides a fundamental information about the energy of the precipitating PsA electrons and wave-particle interacting in the source of PsA.

2 Dataset

2.1 EISCAT Mainland System

This paper is primarily based on analyses of the electron density data from the European Incoherent SCATter (EISCAT) radar system, which has been operative in Tromsø, Norway

(69.60°N, 19.20°E). The EISCAT system in Tromsø consists of two radars, the UHF and VHF radars. The operating frequency of the UHF system is 931 MHz and that of the VHF system is around 224 MHz [*Rishbeth and Williams*, 1985]. The UHF radar data used in the statistical analysis were obtained by the CP-1 (field-aligned stationary experiment), CP-2 (4 direction measurements in the vicinity of the field-aligned direction) and CP-3 (latitudinal scanning experiment) modes. For the analysis of the VHF radar data, we only use data obtained by the vertical stationary experiment mode (CP-6). This mode is designed to probe the D and lower E-region ionosphere (60–140 km altitude), which is particularly suitable for observing ionization due to the hard precipitation associated with PsA. The detail of the EISCAT experiments is provided in http://www.eiscat.se/about/experiments2/scans/.

For conducting the statistical analysis, we converted the original electron density estimates from EISCAT to "reduced data", in which the peak height of the electron density (h_mE) and the electron density at the peak (N_mE) were estimated for every interval of the radar integration time. Since we employed data from several different scanning modes, the data were not always obtained along the magnetic field line or zenith direction. Thus, in the statistical analysis, we only used observations from the field-aligned direction for the UHF radar and zenith direction for the VHF radar. This restriction enables us to compare the occurrence of PsA above Tromsø and the variations of h_mE and N_mE derived from EISCAT. One important point we have to remind is that the temporal resolution of the reduced EISCAT data (h_mE and N_mE) is generally longer than the typical period of PsA. This means that the current statistical analysis provides average characteristics of the electron density profiles over the ON and OFF phases of PsA. To supplement this shortcoming of the statistics, we also carried out some detailed case studies using high-time resolution EISCAT measurements, which can resolve the modulation of ionization associated with PsA.

2.2 Optical Instruments in Tromsø

In Tromsø, a number of all-sky cameras have been operated by National Institute of Polar Research, Japan (NIPR). In particular, high-time resolution optical measurements have been carried out since 2007. In this study, we employed such high-time resolution optical data for checking the occurrence of PsA near the zenith of Tromsø, which corresponds to the looking direction of the EISCAT field-aligned and zenith measurements used in the statistics. For a 3 years period from 2007 to 2009, data from an all-sky TV camera (ATV) were employed for the analysis. The ATV was operated as a campaign basis in winter seasons from 2007 to 2009. The original sampling rate of ATV is $\sim$30 Hz, but, for the purposes of the present study, the original ATV data were digitized once every second. Since 2010, all-sky Watec imagers (AWI) have been operative in Tromsø almost continuously throughout the winter season. We used the green line all-sky images from the AWI system, which were obtained every second with a broad band optical filter ($\sim$500–600 nm) covering the auroral 557.7 nm emission. These green line auroral images from AWI were employed for the later 3 years period of the statistical analysis from 2010 to 2012.

3 Pilot Case Studies

3.1 Overview of PsA Ionization

Before showing the statistical results, we present two case examples of PsA events observed in Tromsø to introduce the dataset used in the analyses. Figure 1 gives a summary of observations of the two EISCAT radars and ATV in Tromsø in the morning of March 9, 2008. This event has already been investigated by *Hosokawa et al.* [2010] and *Hosokawa and Ogawa* [2010]. Figure 1a shows the ATV data in a format of keogram, which is a time-series of the south to north cross section of all-sky images. During the first half of the interval, a very faint east-west aligned arc was seen. This quiet arc moved southward gradually and then led to an intensification of aurora at ∼0145 UT. This intensification ceased once, and then other intensification occurred slightly before 0230 UT. After that, the FOV of the ATV was filled with active discrete aurora until 0250 UT. At around 0250 UT, the form of the aurora suddenly became diffuse. This transition from discrete to diffuse aurora marks the start of PsA which continued until the end of the interval. Since the optical data in Figure 1a are composed of down-sampled 1 min resolution images, we cannot see any signatures of optical pulsation. However, during the 40 min interval from 0250 to 0330 UT, very intense PsA were observed in the entire part of the FOV.

Figures 1b and 1c respectively show the electron density data obtained from the EISCAT UHF and VHF radars as a function of time and altitude. Although these two radars were observing slightly different regions (field-aligned direction for UHF and zenith direction for VHF), overall similarities are seen between the two datasets. For example, both the radars observed remarkable ionization after 0250 UT at altitudes below 100 km, which demonstrates that the PsA electrons were relatively high-energy. Superimposed on these two panels is the peak height (h_mE) derived from the altitude profile of the electron density. The overlaid h_mE values are somewhat affected by the limit of the altitude range of the measurement, especially by the upper limit of the VHF radar. However, the h_mE time-series well traces the height variation of the ionization layer during the interval of PsA, that is, the peak height decreased soon after the start of PsA at 0250 UT. This is a typical response of the electron density in the ionosphere to the occurrence of PsA.

Time-series of N_mE and h_mE estimated from the electron density profiles from UHF (red) and VHF (green) radars are shown in Figures 1d and e, respectively. As mentioned above, h_mE decreased soon after the appearance of PsA. N_mE in Figure 1d was as high as $10^{11.5}$ m^{-3} during the PsA interval, which indicates that the PsA during the current interval was relatively intense. Although the pointing directions of the two radar systems were slightly different, the derived h_mE and N_mE values show overall agreement between the radars. These N_mE and h_mE values are derived with a temporal resolution of 2 min; thus, the slight difference in the pointing direction of the two radars does not introduce a significant offset in h_mE and N_mE. This means that we are able to mix the data from UHF (field-aligned) and VHF (zenith) radars for deriving the statistical characteristics of the PsA ionization. AE index shown in Figure 1f had a peak value of 857 nT at around 0210 UT, which suggests that this PsA event occurred during the recovery phase of a moderately large substorm.

Figure 2 shows another example of the AWI and EISCAT VHF radar data during two separate PsA intervals on January 25, 2012. Figure 2a gives the AWI data in a format of south to north keogram. There were two consecutive intervals of PsA in 03–05 MLT and ~07 MLT. Figure 2b presents the electron density from the zenith measurement of the EISCAT VHF radar. During the first PsA interval, ionization primarily occurred at altitudes between 95 to 140 km. In contrast, during the second PsA interval, the central altitude of the PsA ionization was ~100 km and its lower edge was as low as 80 km altitude. This remarkable difference in the ionization altitude is more clearly seen in the h_mE data shown in Figure 2c, in which the peak of the PsA ionization was mostly above 110 km altitude for the first interval, and ~90 km, well below 100 km, for the second interval. This significant contrast demonstrates that the peak altitude of the PsA ionization may change depending on the magnetic local time where they are observed.

3.2 Pulsating Ionization

To reveal the true altitude profile of the PsA ionization, we have to deal with the electron density data during the ON and OFF phases separately. For this purpose, here we picked up 5 intervals (Intervals I to V) from the 2 events described above, during which high-time resolution (5 sec) EISCAT data are available. In the following, we present the temporal variations of the optical and electron density measurements during the 5 intervals, and derive the true altitude profile of the PsA ionization for each case.

Figure 3 presents data from the first two intervals (Interval I and II) on March 9, 2008. The south to north keogram (top), time-series of the optical intensity at zenith (middle), and the electron density from the EISCAT VHF radar (bottom) are shown. In both the intervals, a series of white stripes and corresponding successive peaks are seen in the keograms and the zenith intensity plots, respectively. These are typical signatures of ON and OFF phases of optical pulsation. The period of these optical pulsations was 5–20 sec. In the EISCAT data on the bottom, we are also able to identify quasi-periodic enhancements of the electron density in the lower E region altitudes below 120 km, which correlate well with the optical pulsations. In the last 1 min period during Interval I, however, there is no clear one-to-one relationship between the optical peaks and the electron density enhancements. This is because the period of the PsA in this 1 min interval was almost comparable or slightly shorter than the recombination time constant in the E region ionosphere (5–10 sec), which did not allow the electron density to respond the fast modulation of the PsA electrons.

Figure 4 introduces another 3 examples of the high-time resolution EISCAT measurements (Interval III to V) from January 25, 2012 event. The plotted parameters and the format of the panels are same as those in Figure 3. During Interval III and IV, clear manifestations of PsA are seen in the optical data in the upper two panels. The EISCAT VHF radar data in the bottom show successive enhancements in the electron density at altitudes between 100 and 120 km, which are very similar to the periodic ionizations during Interval I and II in Figure 3. In these two intervals, the period of the optical pulsations was 15–25 sec, which is well larger than both the recombination time constant in the E region and the temporal resolution of the EISCAT measurements. Thus, the electron density had sufficient time to respond periodic precipitations of the PsA electrons. Important point to note is that the periodic ionization are seen at higher altitudes (above 100 km) during Interval III and IV as compared with that during Interval I and II.

During Interval V, the optical signatures of PsA are somewhat different from those in the previous 4 intervals. Although we can identify indications of pulsation, but the contrast between the ON and OFF phases is relatively unclear. This tendency is clearly seen in the time-series of the zenith intensity in the middle panel. The period of the dominant pulsating component was longer than 30 sec. The EISCAT data in the bottom panel show periodic variations in the electron density mainly below 100 km altitude. The bottom side cut-off of the ionization signatures is ∼82 km, which is almost comparable to the profile during the Interval I and II. Another interesting point to note is that the contrast between the ON and OFF phases of PsA is not clear also in the electron density data. Namely, the behavior of the PsA ionization is in good agreement with the visual characteristics of the optical pulsation.

3.3 True Altitude Profile of PsA Ionization

Hereafter, we try to derive the true altitude profile of the PsA ionization by using the EISCAT data presented in Figures 3 and 4. That is, we pick up several ON and OFF phases of PsA for each interval, and then calculate altitude profiles of the electron density without mixing the ON/OFF phases of PsA. In the left panels of Figure 5, the red (blue) curve gives the average profile during the ON (OFF) phase of PsA for the 5 PsA intervals. In the right panels, the difference between the ON and OFF profiles is presented, which would correspond to the true altitude profile of the PsA ionization. During Interval I and II, there exists a remarkable difference between the ON and OFF profiles. While the peak of the OFF profiles is seen between 110 and 120 km altitude, that of the ON profiles is below 100 km altitude. The difference profiles on the right panels indicate that the PsA ionization occurs in a wide range of altitude from 85 to 110 km, the peak being at somewhere between 90 and 100 km. Thus, the stopping height of the main component of the PsA electrons is between 90 and 100 km. Interesting to note is that the peak of the true altitude profiles of the PsA ionization (90–100 km) is actually ∼10 km lower than the h_mE values shown in Figure 1c (100-120 km). This implies that care must be taken when we derive the characteristic energy of the PsA electrons from the average altitude profile obtained without separating the ON and OFF phases of PsA. In such a case, it might be better to use the cut-off altitude of ionization during the ON phase as a proxy for estimating the energy of PsA electrons.

For Interval III to V, the difference between the ON and OFF profiles is smaller than that during Interval I and II. As mentioned above, the PsA ionization occurred at higher altitude during Interval III and IV. Actually, the peak of the difference profiles is located between 100 and 105 km altitude for these cases. However, these peak altitudes are still slightly lower (∼5 km) than the h_mE values shown in Figure 2c (∼110 km). This again implies that the energy of the PsA electrons can be underestimated if we use an average profile without separating the ON and OFF phases [e.g., *Jones et al.*, 2009]. During Interval V, the peak of the difference profile is located at altitudes between 90 and 95 km. There is ∼10 km difference in the peak height of the PsA ionization between previous events (Interval III and IV) and this event (Interval V). This indicates that the energy of the PsA electrons is highly dependent on the magnetic local time. The other important point is that the difference profiles have a long tail to higher altitude. For example, there exists a small difference between the ON and OFF profiles in Figure 9g although the offset becomes negligible above 130 km altitude. The derivation of the true altitude profile of PsA ionization demonstrates that the peak of ionization during the ON phase of PsA is systematically lower than the h_mE shown in Figures 1 and 2. Hence, when we use the h_mE values in the statistics as proxies for the peak of the PsA ionization, we have to bear in mind that there should exist a 5–10 km offset between the true peak and h_mE.

4 Statistical Analysis

As demonstrated in the previous section, the h_mE values derived without separating the ON and OFF phases of PsA contain non-negligible offset (∼5–10 km) to higher altitudes. However, we used such h_mE values in the statistical analysis in order to reveal average characteristics of PsA. This is primarily because the true peak height of the PsA ionization can be estimated only for limited cases of PsA intervals where the high-time resolution EISCAT data are available. The purpose of this study is to derive the average statistical characteristics of PsA ionization based on a large data set; thus, we carried out the statistics with the reduced h_mE dataset.

4.1 Distribution of Peak Density and Height

To clarify which part of the ionosphere is most affected by the PsA electrons, we investigated the temporal evolution of h_mE during the 21 intervals of PsA selected by the optical observations. Figure 6 shows a summary of the temporal variation of h_mE during the 21 intervals. Red lines show the h_mE values obtained from the UHF radar and the green lines show those from the VHF radar. The temporal resolution of these h_mE time-series is 1–2 min in most cases. But, for the UHF radar data, we only plot data obtained from the measurements of field-aligned direction; thus, the temporal resolution is sometimes very coarse (e.g., Event 13, and 14). During intervals of PsA, which are indicated by the gray shaded areas, h_mE is lower than that during the surrounding non-PsA intervals. The h_mE values are sometimes below 100 km during PsA. This tendency is more clearly seen in Event 02, 17, 19, and 21, which occurred in the morning side. However, there are some exceptions in which h_mE remains high, above 110 km, even during PsA (e.g., Event 09, 12, 15, 16, 18, and 20). These events were commonly observed in earlier local time sector.

In order to see the occurrence distribution of N_mE and h_mE during PsA, we statistically analyzed the relationship between N_mE and h_mE during the 21 intervals. The results are shown in Figure 7b. It is clearly seen that the peak electron density is larger when the peak of ionization occurs at lower altitude. Figures 7a and 7c respectively provide the distribution of N_mE and h_mE. The majority of N_mE is distributed between $10^{11.0}$ to $10^{11.8}$ m^{-3}. These values are almost comparable to the ionization due to discrete aurora [e.g., *Oyama et al.*, 2014]. The occurrence peak of h_mE is located between 110 and 115 km, but there is a population below 100 km. This peak height of the PsA ionization is slightly lower than that of discrete aurora [e.g., *Oyama et al.*, 2014]. However, the difference is not as significant as expected, which is probably because we mix the ON and OFF phases of PsA in this statistics because the temporal resolution of the h_mE data is well longer than the typical period of PsA (a few to a few tens of sec).

4.2 Dependence of PsA Ionization on MLT

In Figure 2, we briefly mentioned that the peak of the PsA ionization tends to be lower in the morning side. To confirm this characteristics, we show the occurrence distribution of h_mE during the 21 PsA intervals as a function of MLT in Figure 8. Figure 8a presents the distribution of the h_mE data point used in the statistics, which is equivalent to the MLT distribution of the PsA occurrence. As shown in *Oguti et al.* [1981] and *Jones et al.* [2011], PsA typically occur in the morning side. In our database, almost all the data point are distributed from magnetic midnight to 08 MLT, the peak being at around 03 MLT. This is fairly consistent with the past statistical studies of PsA. In Figure 8b, the occurrence distribution of h_mE is plotted as a function of MLT. Before 05 MLT, the peak is located between 110 to 120 km altitude. In contrast, the peak of the h_mE occurrence becomes lower below 100 km after 06 MLT. This infers that the energy of the PsA electrons becomes higher in the morning side than that in the post-midnight sector.

4.3 Dependence of PsA Ionization on AE Index

Now we turn to examine the dependence of h_mE and N_mE during PsA on the magnitude of preceding substorms. Here, we divide all the 21 PsA intervals into three broad categories: small substorm (AE $<$ 200 nT: blue), moderate substorm (200 $<$ AE $<$ 500 nT: green) and large substorm (AE $>$ 500 nT: red) and plot the occurrence of h_mE and N_mE in Figure 9. The PsA ionization is more intense (N_mE is larger) and occurs at lower altitude (h_mE is lower) when the peak AE index during the preceding substorms is larger. This tendency might reflect the characteristics of the amount energy of source electrons and intensity of the waves in the source of PsA in the magnetosphere. The data points of the high-altitude ionization for the larger substorm mostly come from Event 20 on January 25, 2012, which was already shown in Figure 2. During this particular event, h_mE remained high even during PsA. This is possibly because this PsA event occurred in the earlier MLT sector; thus, the altitude of the PsA ionization is higher even though a relatively larger substorm occurred before PsA.

5 Discussion

One of the main purposes of this study is to reveal the height profile of the PsA ionization. We found that there is a non-negligible difference between the average altitude profile derived from the coarse data and the true altitude profile estimated by separating the ON and OFF phases of PsA. Thus, the height distribution of h_mE shown in Figure 7c contains slight offsets to higher altitudes. This means that the use of such smoothed h_mE values could lead to an underestimation of the characteristic energy of PsA electrons. That is, when we use the height profile of the electron density from IS radars for estimating the energy of PsA electrons, the separation of the ON and OFF phases of PsA is crucial. In recent years, several authors tried to derive the energy spectra of PsA electrons by using IS radar data [*Jones et al.*, 2009; *Miyoshi et* *al.*, 2015]. Since these authors did not distinguish the ON and OFF phases of PsA in their analyses, the estimated characteristic energy of PsA electrons could be underestimated. Especially, *Miyoshi et al.* [2015] employed the EISCAT VHF radar experiment to detect precipitation of sub-relativistic electrons (∼200 keV) during PsA. If they were able to separate the spectra during the ON and OFF phases of PsA, the maximum energy of PsA precipitation could be further higher. In the future study, we need to investigate the low-altitude ionization during PsA by considering the ON and OFF phases of optical pulsation.

The peak of the true altitude profiles during Interval I, II and V shown in Figure 5 was located at altitudes of 90-100 km, which corresponds to the energy of incident electrons of 10–30 keV [e.g., *Rees*, 1963]. This central energy of PsA electrons is roughly consistent with the past in-situ rocket observations by *Sandahl et al.* [1980] and *Yau et al.* [1981] who detected pulsating precipitation of electrons with energies from a few keV to tens of keV during intervals of PsA. The true altitude profiles for these cases have a tail at least down to ∼80 km altitude, which corresponds to an energy of electrons of ∼100 keV. Recently, several in-situ observations of the PsA electrons were made by using data from the Reimei satellite [*Miyoshi et al.*, 2010; *Nishiyama et al.*, 2011]. The upper limit of the electron detector onboard Reimei is 12 keV, but, these authors indicated that electrons having much higher energy should have precipitated into the region of PsA. Recently, *Miyoshi et al.* [2015] detected, by using the EISCAT data, an electron density enhancement at ∼68 km altitude during PsA, which corresponds to precipitation of ∼200 keV electrons. In the current study, we confirmed the existence of high-energy PsA electrons up to ∼100 keV. Such high-energy electrons might have contributed to an enhancement of NO_x and subsequent depletion of stratospheric Ozone [e.g., *Thorne*, 1977; *Isono et al.*, 2014]; thus, they would be of particular importance for understanding the impact of PsA on the middle atmosphere.

In the past literature, *Stenbaek-Nielsen and Hallinan* [1979] reported that patches of

PsA are sometimes as thin as ∼2 km in altitude. In contrast to such observations of thin PsA, our measurements, for example those shown in Figure 5, demonstrated that the layer of PsA ionization had a thickness of ∼20–30 km. Such thick layer of PsA ionization was already reported by *Jones et al.* [2009] who showed that the PsA patches had a thickness of ∼15–25 km in all the cases they analyzed. The present study confirmed this characteristics by separating the true altitude profiles of ionization during the ON and OFF phases of PsA; thus, the thin PsA patch reported by *Stenbaek-Nielsen and Hallinan* [1979] is only a class (probably not dominant) of PsA. The derived thick ionization layer indicates that the energy spectra of PsA electrons are basically broad from a few to a few tens of keV. Such a broad spectra of the PsA electrons can be explained by a time-of-flight model of wave particle interaction by *Miyoshi et al.* [2010]. Since the resonant energy of the wave-particle interaction depends on the magnetic latitude, electrons in a wide range of energy can be scattered by whistler mode chorus waves propagating along the field-lines. *Miyoshi et al.* [2010] employed this model to understand the energy dispersion of PsA electrons observed by the Reimei satellite. But, the idea can also be used for explaining the broad energy spectra of PsA electrons inferred by the current study.

As discussed above, the average altitude profile (h_mE and N_mE) used in the statistics contains some sort of uncertainty in estimating the characteristic energy of PsA electrons. However, the results of the statistics can be used at least for discussing the dependence of the PsA ionization on MLT and AE index. Figure 8 shows that most of the data points (i.e., occurrence of PsA) are distributed in the post-midnight to morning local time sector (00 to 08 MLT). This occurrence distribution of PsA is consistent with the past statistical analysis of PsA based on the ground-based optical data [*Kvifte and Pettersen*, 1969; *Oguti et al.*, 1981; *Jones et al.*, 2011] and can be simply associated with the global distribution of whistler-mode chorus waves in the magnetosphere [e.g., *Thorne et al.*, 2010; *Li et al.*, 2009]. The other important point in Figure 8 is that the central altitude of the PsA ionization decreases, i.e., the energy of

PsA electrons becomes harder, in the later MLT sector away from the midnight. We speculate that this characteristic MLT dependence of the energy of PsA electrons can be explained by an increase of the resonance energy of the pitch angle scattering process in the later MLT sector.

The parallel resonance energy of the first order cyclotron resonant scattering is known to be proportional to the square of the ambient magnetic field intensity [*Kennel and Petschek*, 1966]. The magnetic field intensity at a conjugate point of Tromsø in the magnetic equator can be estimated to be ~25 nT at 0130 UT (04 MLT) and ~52 nT at 0430 UT (07 MLT) for January 25, 2012 event shown in Figure 2 [*Tsyganenko and Sitnov*, 2005]. That is, the magnetic field intensity at the magnetic equator is twice larger at 07 MLT than that 04 MLT. This leads to a difference in the resonance energy, and then the energy of the PsA electrons tends to be larger in the later MLT sector. This result implies that the current EISCAT measurements provide an important clue for the wave-particle interaction in the magnetosphere and the formation of diffuse auroral precipitation.

In Figure 9, we demonstrated that, when the AE index of the preceding substorm is larger, h_mE is lower and N_mE is larger. This suggests that the flux of PsA electrons is larger and their energy is higher during geomagnetically disturbed conditions. Many of the previous satellite observations in the magnetosphere [*Li et al.*, 2009, *Thorne et al.*, 2010; *Meredith et al.*, 2012] showed that the whistler mode chorus is more intense when the AE index is larger. The current statistical analysis of the EISCAT data is consistent with these previous satellite observations of the chorus waves in the magnetosphere. This supports the idea that the pitch angle scattering by the whistler mode chorus precipitates the PsA electrons into the ionosphere. However, there is an exception during the first half of the January 25, 2012 event. During this event, the central altitude of the PsA ionization was high even though the peak AE index of the preceding substorm was relatively large. This is primarily because this event occurred in the earlier MLT sector in which the PsA electrons tend to be softer. This again implies that the MLT is one of the most important factors controlling the energy of the PsA electrons.

Recently, *Hosokawa et al.* [2010] implied an existence of electric field modulation within patches of PsA. They explained this variation by a polarization electric field created by a conductivity enhancement within the PsA patches. They also demonstrated that about 30% of the polarization charges accumulated at the edges of the PsA patches should escape from the ionosphere as field-aligned current (FAC). In the past, the existence of such a PsA associated FAC system was reported by *Fujii et al.* [1985] who employed the MAGSAT satellite magnetic field measurements to identify a signature of FAC in the vicinity of patches of PsA. They clearly demonstrated that signatures of FAC varied in harmony with optical pulsation observed on the ground, and then inferred that the PsA associated FAC is closed via enhanced Pedersen current flowing within the PsA patches. Their results indicate that the ionospheric electrodynamics associated with PsA may modify the magnetosphere-ionosphere coupling systems with a period of optical pulsation.

We showed in Figure 7 that there is a relationship between N_mE and h_mE, that is, the enhancement of the electron density is larger when the height of the ionization is lower. This means that the modification of the ionospheric electrodynamics is much more significant when the ionization layer is in the lower E region. In such situations, pulsating ionization occurs only below 110 km; thus, only the Hall conductance is enhanced and the Pedersen current does not change in association with PsA. This means that the polarization at the edges of PsA patches occurs mainly due to the enhancement of Hall conductance. *Fujii et al.* [1985] claimed that the variation of FAC above PsA patches is produced by an enhanced Pedersen current within patches. However, this should not be the case for most of PsA events because the electric current flowing in the Pedersen layer does not change during the ON and OFF phases of PsA. In reality, the enhancement of Hall conductance in the lower E region within patches of PsA should be the origin of PsA associated FAC observed by *Fujii et al.* [1985].

6 Summary

Variation of the ionospheric electron density profile during PsA was statistically investigated by using EISCAT radar in Tromsø, Norway. The results of the statistical analysis can be summarized as follows:

1. The energy of incident electrons is higher during the periods of PsA than that in the non-PsA intervals, which is consistent with past in-situ measurements of high-energy precipitating electrons by sounding rockets during intervals of PsA [e.g., *Sandahl et al.*, 1980].

2. The energy of PsA electrons tends to be higher in the later MLT sector away from the magnetic midnight. This tendency can be explained by an increase of resonance energy of the wave-particle interaction due to the larger magnetic field intensity in the morning side.

3. When the AE index during the preceding substorm is larger, the PsA electrons are harder and their flux is larger. This is in good agreement with the enhancement of whistler mode chorus waves in the magnetosphere shown by recent satellite measurements in the magnetosphere.

In addition to the statistics using the EISCAT data, we carried out several detailed case studies, in which the altitude profiles of the PsA ionization were derived by separating the ON and OFF phases of PsA. The case studies showed that there is a non-negligible difference between the average altitude profile derived from the coarse data and the true altitude profile estimated by separating the ON and OFF phases of PsA. That is, when we use the height profile of electron density from IS radars for estimating the energy of PsA electrons, the separation of the ON and OFF phases of PsA is crucial. The estimated true altitude profile shows an enhancement of the electron density down to 80 km altitude, which corresponds to energy of 100 keV electrons. This again implies that the energy of PsA electrons is much harder than that of the discrete aurora.

Acknowledgment. We are indebted to the director and staff of EISCAT for operating the facility and supplying the data. EISCAT is an International Association supported by China (CRIRP), Finland (SA), Germany (DFG), Japan (NIPR and STEL, Nagoya), Norway (NFR), Sweden (VR) and the United Kingdom (PPARC).

References

Bosinger, T., K. Kaila, R. Rasinkangas, P. Pollari, J. Kangas, V. Trakhtengerts, A. Demekhov, T. Turunen (1996), An EISCAT study of a pulsating auroral arc: simultaneous ionospheric electron density, auroral luminosity and magnetic field pulsations, *Journal of Atmospheric and Terrestrial Physics, 58*, 23–35.

Fujii, R., T. Oguti, and T. Yamamoto (1985), Relationships between pulsating auroras and field-aligned electric currents, *Mem. Nat'l Inst. Polar Res., 36*, 95–103.

Hargreaves, J. K., M. J. Birch, and B. J. I. Bromage (2007), D- and E-region effects in the auroral zone during a moderately active 24-h period in July 2005 *Ann. Geophys., 25*, 1837–1849.

Hosokawa, K., Y. Ogawa, A. Kadokura, H. Miyaoka, and N. Sato (2010), Modulation of ionospheric conductance and electric field associated with pulsating aurora, *J. Geophys. Res., 115*, doi:10.1029/2009JA014683.

Hosokawa, K., and Y. Ogawa (2010), Pedersen current carried by electrons in auroral D-region, *Geophys. Res. Lett., 37*, L18103, doi:10.1029/2010GL044746.

Johnstone, A. D. (1983), The mechanism of pulsating aurora, *Ann. Geophys., 1*, 397–410.

Jones, S. L., M. R. Lessard, P. A. Fernandes, D. Lummerzheim, J. L. Semeter, C. J. Heinselman, K. A. Lynch, R. G. Michell, P. M. Kintner, H. C. Stenbaek-Nielsen, and K. Asamura (2009), PFISR and ROPA observations of pulsating aurora, *J. Atmos. Solar-Terr. Phys., 71*, 708.

Jones, S. L., M. R. Lessard, K. Rychert, E. Spanswick, and E. Donovan (2011), Large-scale aspects and temporal evolution of pulsating aurora, *J. Geophys. Res., 116*, A03214, doi:10.1029/2010JA015840.

Kvifte, G. J., and H. Pettersen (1969), Morphology of the pulsating aurora, *Planet. Space Sci., 17*, 1599–1607, doi:10.1016/0032-0633(69)90148-2.

Lessard, M. R. (2012), A Review of Pulsating Aurora, in Auroral Phenomenology and Magnetospheric Processes: Earth And Other Planets (eds A. Keiling, E. Donovan, F. Bagenal and T. Karlsson), American Geophysical Union, Washington, D. C.. doi: 10.1029/2011GM001187.

Li, W., R. M. Thorne, V. Angelopoulos, J. Bortnik, C. M. Cully, B. Ni, O. LeContel, A. Roux, U. Auster, and W. Magnes (2009b), Global distribution of whistler-mode chorus waves observed on the THEMIS spacecraft, *Geophys. Res. Lett., 36*, L09104, doi:10.1029/2009GL037595.

Li, W., Bortnik, J., Nishimura, Y., Thorne, R. M. and Angelopoulos, V. (2012), The Origin of Pulsating Aurora: Modulated Whistler Mode Chorus Waves, in Auroral Phenomenology and Magnetospheric Processes: Earth And Other Planets (eds A. Keiling, E. Donovan, F. Bagenal and T. Karlsson), American Geophysical Union, Washington, D. C.. doi: 10.1029/2011GM001164.

Meredith, N. P., R. B. Horne, A. Sicard-Piet, D. Boscher, K. H. Yearby, W. Li, and R. M. Thorne (2012), Global model of lower band and upper band chorus from multiple satellite observations, *J. Geophys. Res., 117*, A10225, doi:10.1029/2012JA017978.

Miyoshi, Y., Y. Katoh, T. Nishiyama, T. Sakanoi, K. Asamura, and M. Hirahara (2010), Time of flight analysis of pulsating aurora electrons, considering wave-particle interactions with propagating whistler mode waves, *J. Geophys. Res., 115*, A10312, doi:10.1029/2009JA015127.

Nishiyama, T., T. Sakanoi, Y. Miyoshi, Y. Katoh, K. Asamura, S. Okano, and M. Hirahara (2011), The source region and its characteristic of pulsating aurora based on the Reimei observations, *J. Geophys. Res., 116*, A03226, doi:10.1029/2010JA015507.

Oguti, T., S. Kokubun, K. Hayashi, K. Tsuruda, S. Machida, T. Kitamura, O. Saka, and T. Watanabe (1981), Statistics of pulsating auroras on the basis of all-sky TV data from five stations. I. Occurrence frequency, *Can. J. Phys., 59*, 1150–1157, doi:10.1139/p81-152.

Oyama, S., Y. Miyoshi, K. Shiokawa, J. Kurihara, T. T. Tsuda, and B. J. Watkins (2014), Height-dependent ionospheric variations in the vicinity of nightside poleward expanding aurora after substorm onset, *J. Geophys. Res. 119*, 4146–4156, doi:10.1002/2013JA019704.

Rees, M. H. (1963), Auroral ionization and excitation by incident energetic electrons, *Planet. Space Sci., 11*, 1209–1218.

Rishbeth, H., and P. J. S. Williams (1985), The EISCAT ionospheric radar: The system and its early results, *Q. J. R. Astron. Soc., 26*, 478–512.

Sandahl, I., L. Eliasson, and R. Lundin (1980), Rocket observations of precipitating electrons over a pulsating aurora, *Geophys. Res. Lett., 7,* 309–312.

Sato, N., D. M. Wright, C. W. Carlson, Y. Ebihara, M. Sato, T. Saemundsson, S. Milan, and M. Lester (2004), Generation region of pulsating aurora obtained simultaneously by the FAST satellite and a Syowa-Iceland conjugate pair of observatories, *J. Geophys. Res., 109*, doi:10.1029/2004JA010419.

Thorne, R. M. (1977), Energetic radiation belt electron precipitation: a natural depletion mechanism for stratospheric ozone, *Science, 195*, 287–289.

Thorne, R. M., B. Ni, X. Tao, R. B. Horne, and N. P. Meredith (2010), Scattering by chorus waves as the dominant cause of diffuse auroral precipitation, *Nature, 467*, doi:10.1038/nature09467.

Wahlund, J.-E., H. J. Opgenoorth, and P. Rothwell (1989), Observations of Thin Auroral Ionization Layers by EISCAT in Connection With Pulsating Aurora, *J. Geophys. Res., 94*, 17,223–17,233.

Yamamoto, T. (1988), On the temporal fluctuations of pulsating auroral luminosity, *J. Geophys. Res., 93*, 897–911.

Yau, A. W., B. A. Whalen, and D. J. McEwen (1981), Rocket-borne measurements of particle pulsation in pulsating aurora, *J. Geophys. Res., 86*, 5673–5681, doi:10.1029/JA086iA07p05673.

Figure Captions

Figure 1 (a) Keogram of Tromsø ATV along the South to North cross section for the interval from 0000 UT to 0330 UT on March 9, 2008. The interval of PsA is indicated by the red bar. (b) Altitude-Time-Intensity plot of the electron density obtained by the EISCAT UHF radar. Superimposed is the peak height (h_mE) estimated every 90 sec. (c) Altitude-Time-Intensity plot of the electron density obtained by the EISCAT VHF radar. Superimposed is the peak height (h_mE) estimated every 90 sec. (d) Time-series of the electron density at the peak height (N_mE) estimated from the EISCAT UHF (red) and VHF (green) radars. (e) Time-series of the peak height (h_mE) estimated from the EISCAT UHF (red) and VHF (green) radars. (f) Providional AE index, the peak during the current 3-h interval was 857 nT.

Figure 2 (a) Keogram of Tromsø AWI along the South to North cross section for the interval from 0000 UT to 0500 UT on January 25, 2012. The intervals of PsA are indicated by the red bars. (b) Altitude-Time-Intensity plot of the electron density obtained by the EISCAT VHF radar. (c) Time-series of the peak height (h_mE) estimated from the altitude profiles of the EISCAT electron density.

Figure 3 (Top) Keogram of Tromsø ATV along the South to North cross section for Interval I and II, respectively. (Middle) Time-series of the ATV optical intensity at zenith for Interval I and II, respectively. (Bottom) Altitude-Time-Intensity plot of the electron density obtained by the EISCAT VHF radar for Interval I and II, respectively.

Figure 4 (Top) Keogram of Tromsø AWI along the South to North cross section for Interval III, IV and V, respectively. (Middle) Time-series of the AWI optical intensity at zenith for Interval III, IV and V, respectively. (Bottom) Altitude-Time-Intensity plot of the electron density obtained by the EISCAT VHF radar for Interval III, IV and V, respectively.

Figure 5 (Left) Altitude profile of the electron density during the ON (red) and OFF (blue) phases of Psa for Interval I to V, respectively. (Right) Difference between the ON and OFF profiles in the left panel, which corresponds to the true altitude profile of the electron density at the time of PsA.

Figure 6 Overview of the temporal evolution of h_mE for the 21 PsA events. The intervals of PsA defined by the simultaneous optical observations are shaded with gray color. The red (green) curve shows the h_mE estimates from the EISCAT UHF (VHF) radar.

Figure 7 (a) Distribution of N_mE during the 21 intervals of PsA. Only the h_mE values obtained when PsA were observed above Tromsø are used, the total number of points being 589. (b) Relationship between N_mE and h_mE during the same intervals of PsA. (c) Distribution of h_mE during the same intervals of PsA.

Figure 8 (a) MLT distribution of the occurrence of the h_mE data points during the 21 intervals of PsA. The total number of points is 589. (b) MLT distribution of altitude distribution of h_mE during the 21 intervals of PsA. The occurrence is self-normalized.

Figure 9 Dependence of N_mE and h_mE on the magnitude of the preceding substorm. The color indicates the three levels of substorm magnitude determined by the peak AE index during the preceding substorm: small (AE $<$ 200 nT), moderate (200 nT $<$ AE $<$ 500 nT) and large (AE $>$ 500 nT).

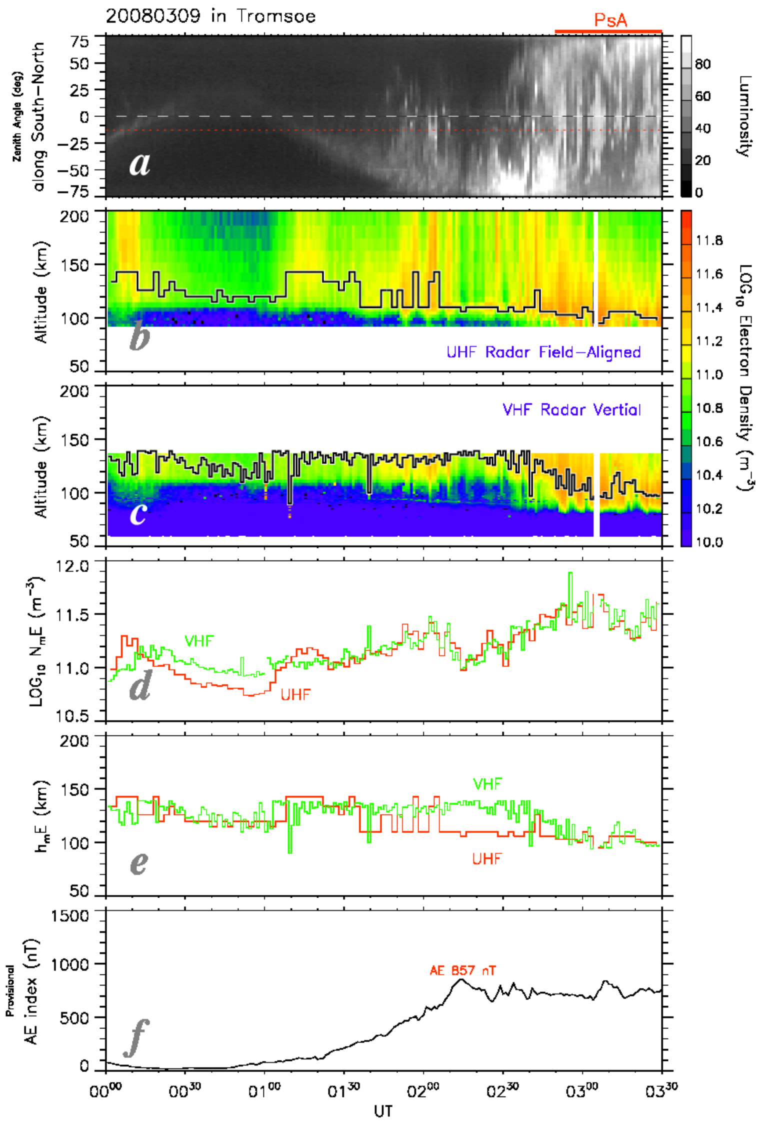

Figure 1: (a) Keogram of Tromsø ATV along the South to North cross section for the interval from 0000 UT to 0330 UT on March 9, 2008. The interval of PsA is indicated by the red bar. (b) Altitude-Time-Intensity plot of the electron density obtained by the EISCAT UHF radar. Superimposed is the peak height (h_mE) estimated every 90 sec. (c) Altitude-Time-Intensity plot of the electron density obtained by the EISCAT VHF radar. Superimposed is the peak height (h_mE) estimated every 90 sec. (d) Time-series of the electron density at the peak height (N_mE) estimated from the EISCAT UHF (red) and VHF (green) radars. (e) Time-series of the peak height (h_mE) estimated from the EISCAT UHF (red) and VHF (green) radars. (f) Providional AE index, the peak during the current 3-h interval was 857 nT.

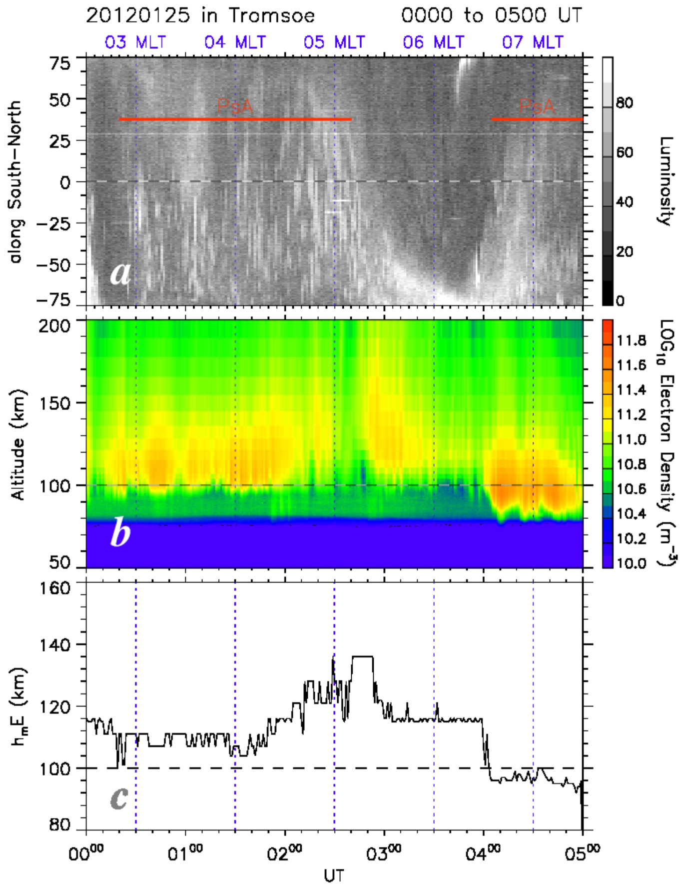

Figure 2: Dependence of N_mE and h_mE on the magnitude of the preceding substorm. The color indicates the three levels of substorm magnitude determined by the peak AE index during the preceding substorm: small (AE $<$ 200 nT), moderate (200 nT $<$ AE $<$ 500 nT) and large (AE $>$ 500 nT).

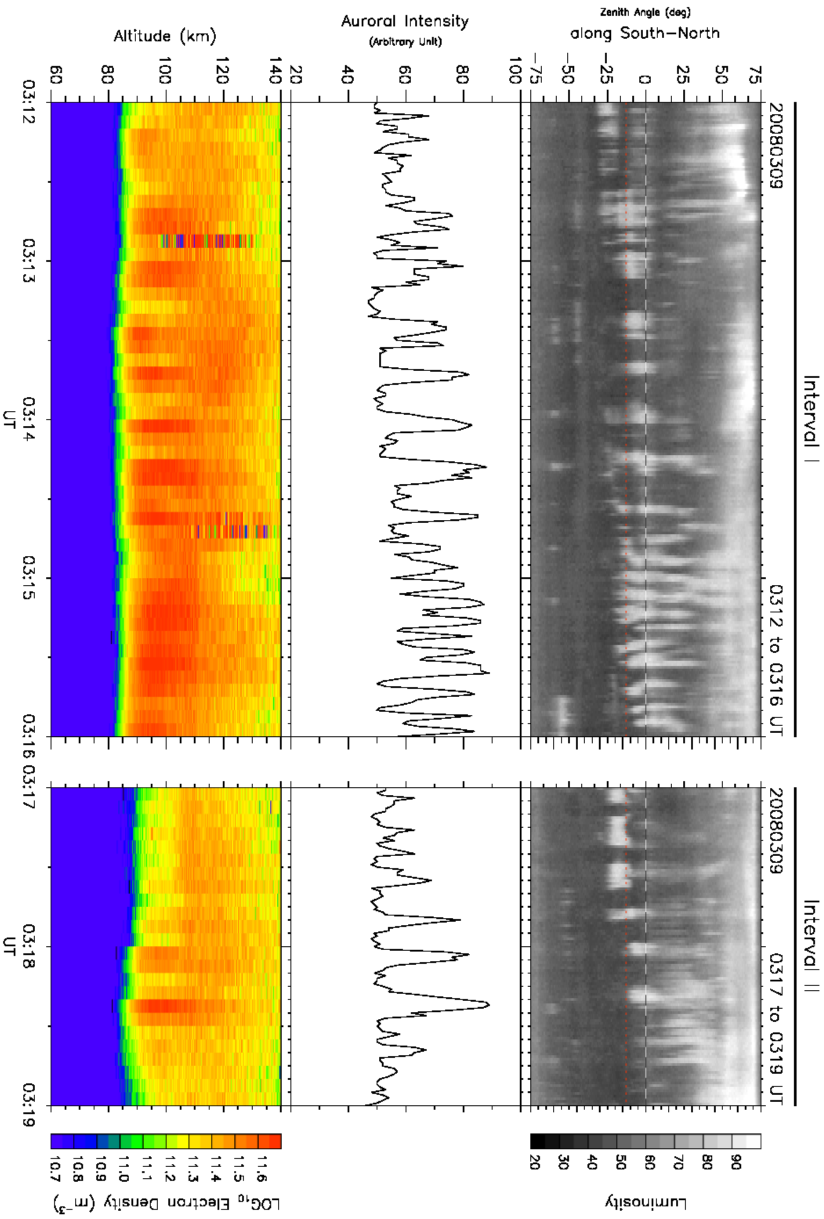

Figure 3: (Top) Keogram of Tromsø ATV along the South to North cross section for Interval I and II, respectively. (Middle) Time-series of the ATV optical intensity at zenith for Interval I and II, respectively. (Bottom) Altitude-Time-Intensity plot of the electron density obtained by the EISCAT VHF radar for Interval I and II, respectively.

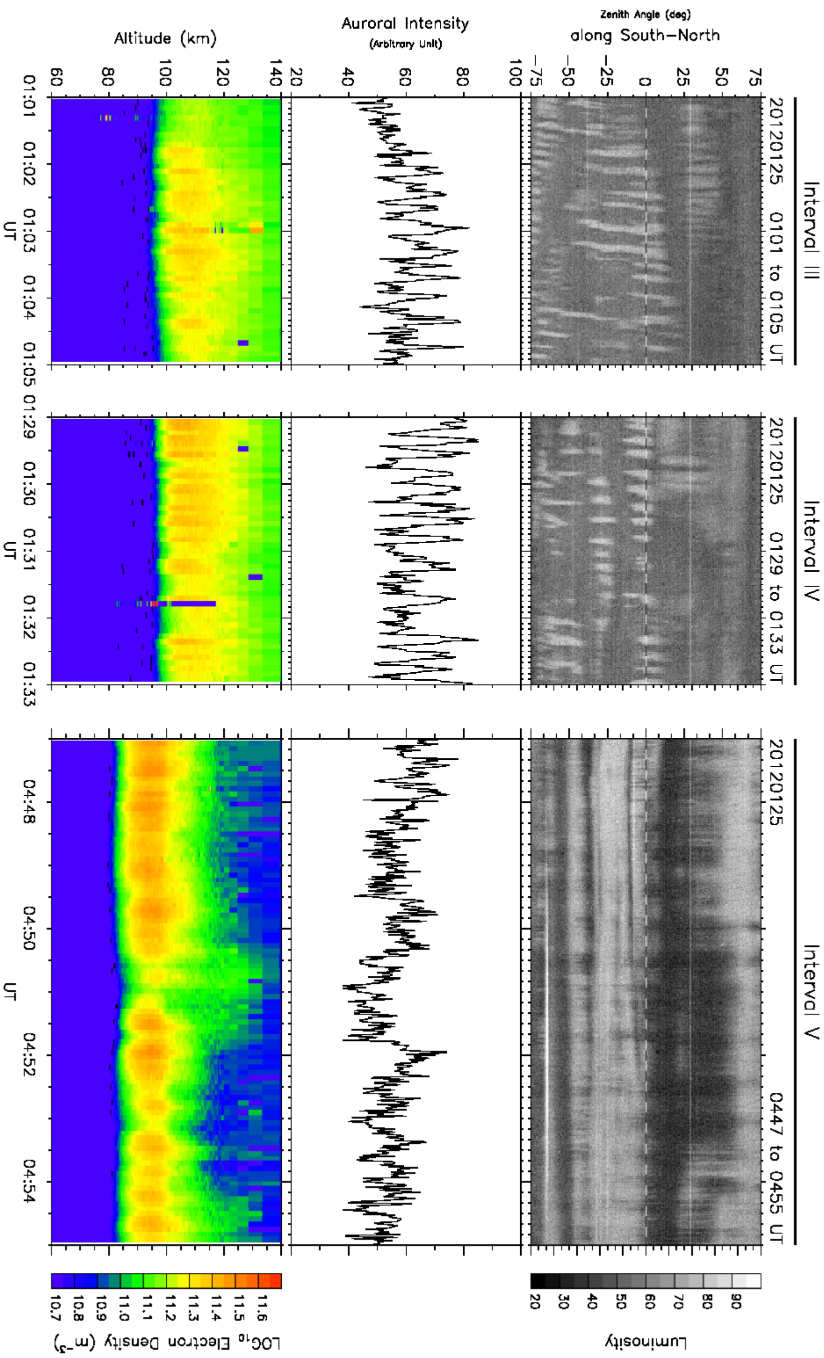

Figure 4: (Top) Keogram of Tromsø AWI along the South to North cross section for Interval III, IV and V, respectively. (Middle) Time-series of the AWI optical intensity at zenith for Interval III, IV and V, respectively. (Bottom) Altitude-Time-Intensity plot of the electron density obtained by the EISCAT VHF radar for Interval III, IV and V, respectively.

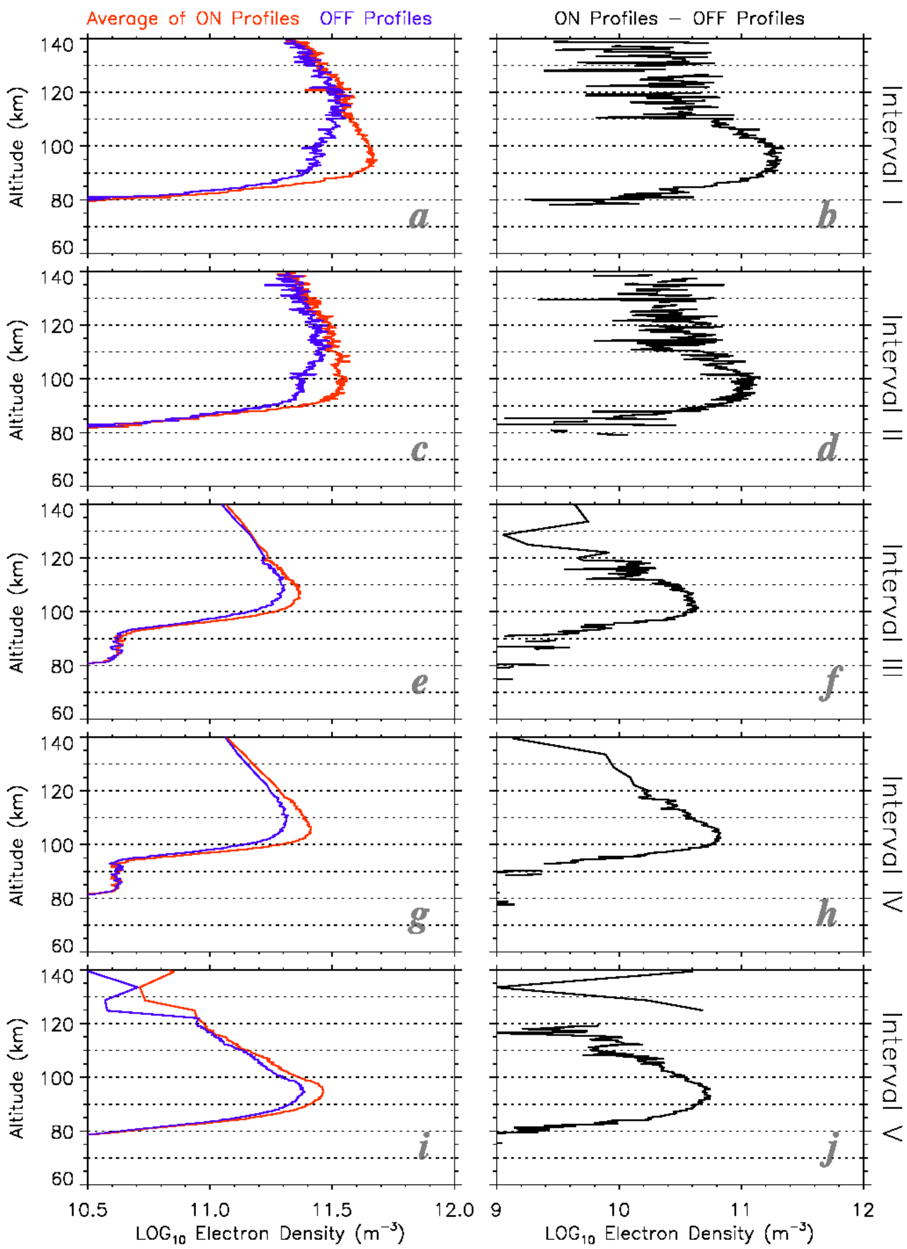

Figure 5: (Left) Altitude profile of the electron density during the ON (red) and OFF (blue) phases of Psa for Interval I to V, respectively. (Right) Difference between the ON and OFF profiles in the left panel, which corresponds to the true altitude profile of the electron density at the time of PsA.

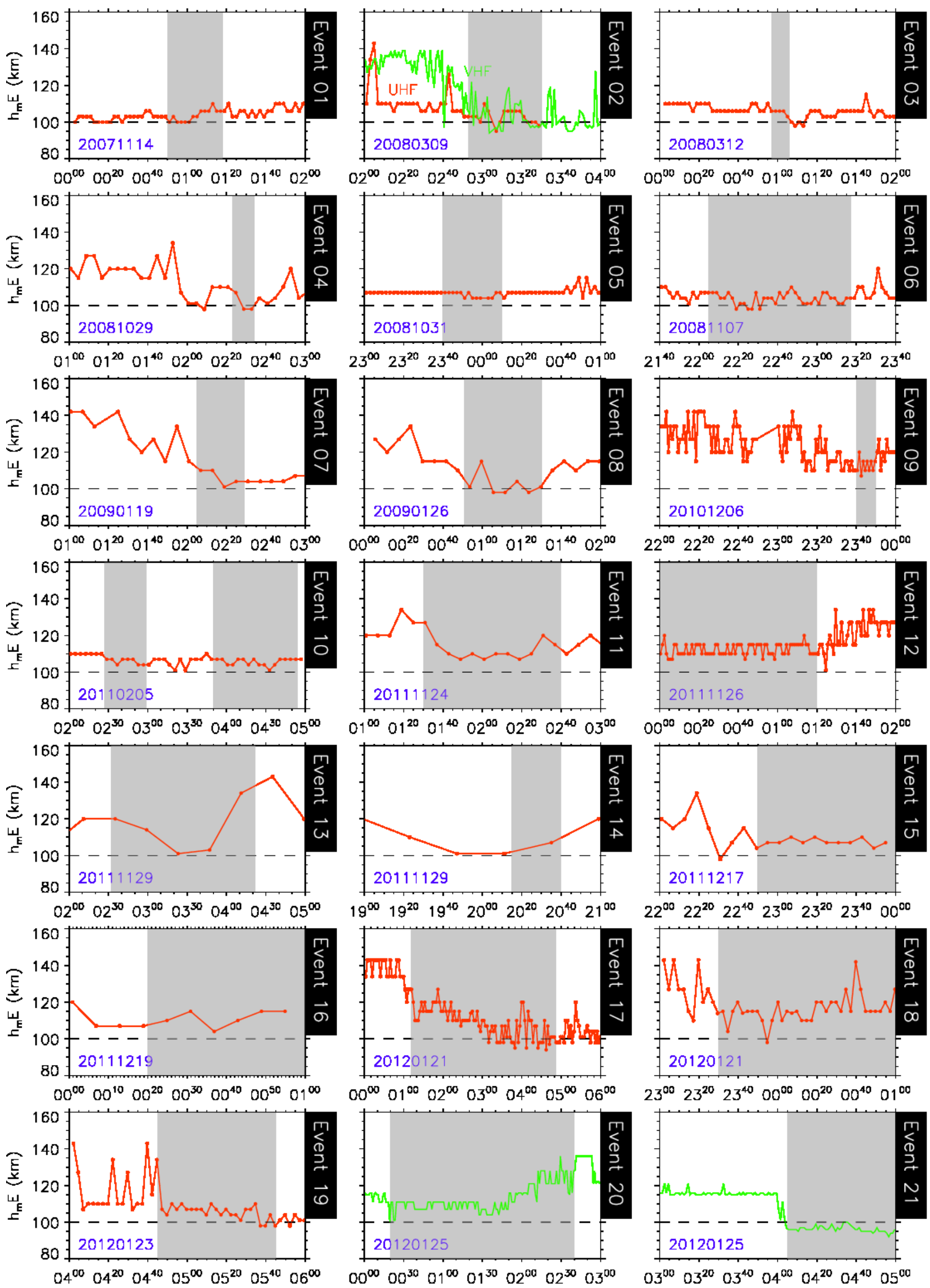

Figure 6: Overview of the temporal evolution of h_mE for the 21 PsA events. The intervals of PsA defined by the simultaneous optical observations are shaded with gray color. The red (green) curve shows the h_mE estimates from the EISCAT UHF (VHF) radar.

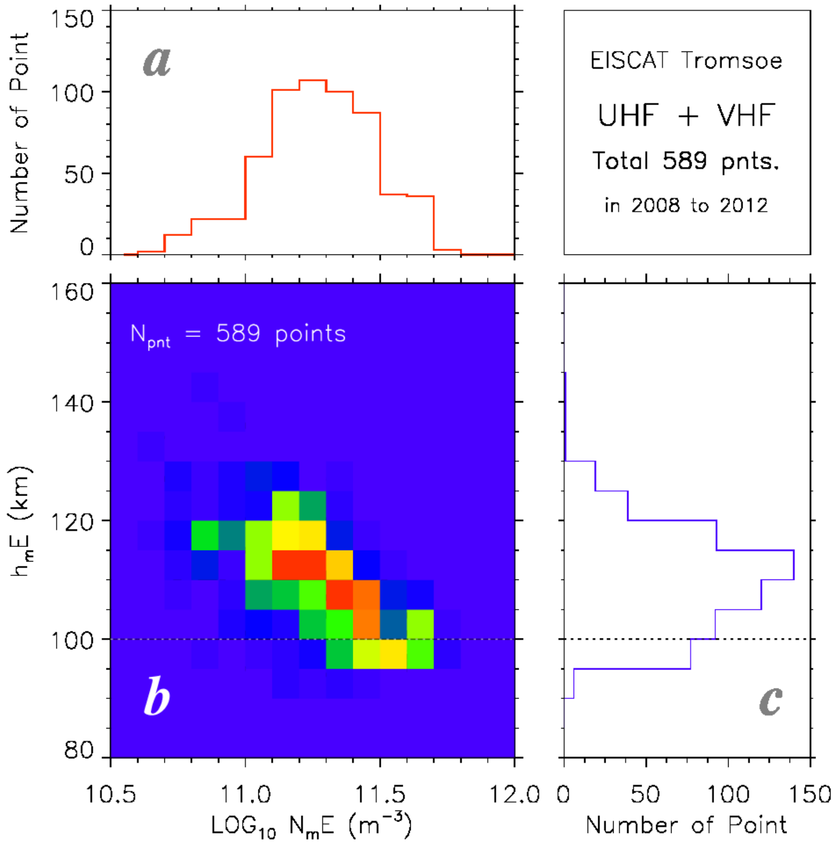

Figure 7: (a) Distribution of N_mE during the 21 intervals of PsA. Only the h_mE values obtained when PsA were observed above Tromsø are used, the total number of points being 589. (b) Relationship between N_mE and h_mE during the same intervals of PsA. (c) Distribution of h_mE during the same intervals of PsA.

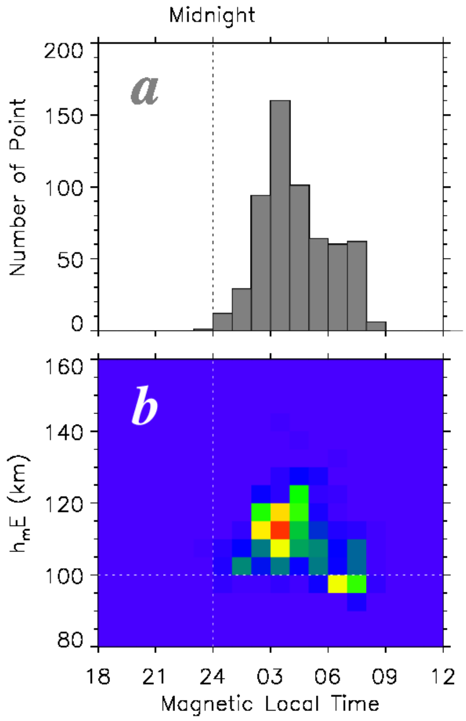

Figure 8: (a) MLT distribution of the occurrence of the h_mE data points during the 21 intervals of PsA. The total number of points is 589. (b) MLT distribution of altitude distribution of h_mE during the 21 intervals of PsA. The occurrence is self-normalized.

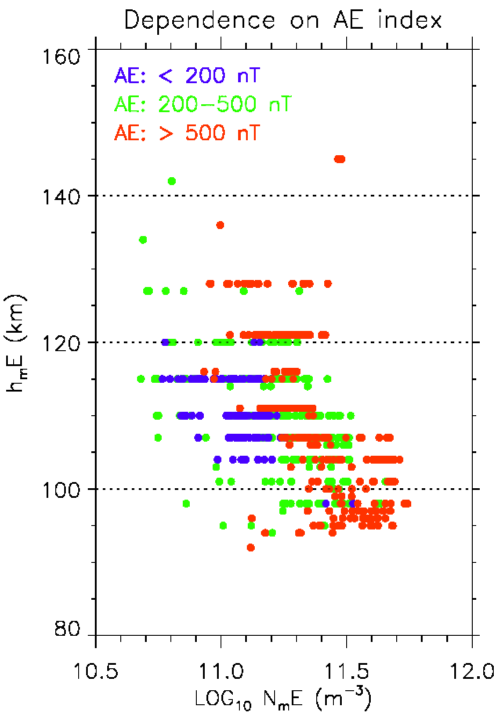

Figure 9: (a) Keogram of Tromsø AWI along the South to North cross section for the interval from 0000 UT to 0500 UT on January 25, 2012. The intervals of PsA are indicated by the red bars. (b) Altitude-Time-Intensity plot of the electron density obtained by the EISCAT VHF radar. (c) Time-series of the peak height (h_mE) estimated from the altitude profiles of the EISCAT electron density.